Published in "ACS Nano 14(2): 1879–1887, 2020"
which should be cited to refer to this work.

http://doc.rero.ch

Colloidal Transformations in MS2 Virus Particles: Driven by pH, Influenced by Natural Organic Matter

Samuel Watts, Timothy R. Julian, Katharina Maniura-Weber, Thomas Graule, and Stefan Salentinig*

ABSTRACT: **Enteric viruses, such as enterovirus, norovirus, and rotavirus, are among the leading causes of disease outbreaks due to contaminated drinking and recreational water. Viruses are difficult to remove from water through filtration based on physical size exclusion—for example by gravity-driven filters—due to their nanoscale size. To understand virus removal in drinking water treatment systems, the colloidal nanostructure of a model virus, the MS2 bacteriophage, has been investigated in relation to the effect of pH and natural organic matter in water. Dynamic light scattering, small-angle X-ray scattering, and cryogenic transmission electron microscopy demonstrated that the water pH has a major influence on the colloidal structure of the virus: The bacteriophage MS2's structure in water in the range pH = 7.0 to 9.0 was found to be spherical with core−shell-type structure with a total diameter of 27 nm and a core radius of around 8 nm. Reversible transformations from 27 nm particles at pH = 7.0 to micrometer-sized aggregates at pH = 3.0 were observed. In addition, the presence of natural organic matter that simulates the organic components present in surface water was found to enhance repulsion between virus particles, reduce the size of aggregates, and promote disaggregation upon pH increase. These findings allow a better understanding of virus interactions in water and have implications for water treatment using filtration processes and coagulation. The results will further guide the comprehensive design of advanced virus filter materials.**

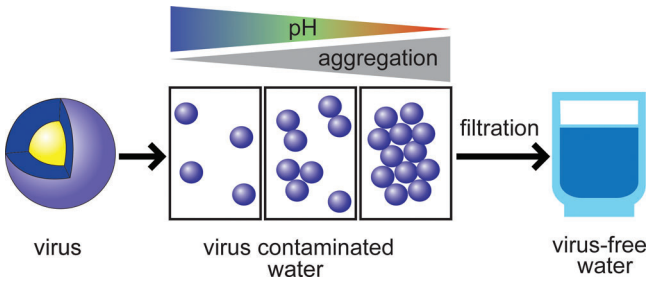

KEYWORDS: *pH triggered virus aggregation, bacteriophage MS2, water filtration, self-assembly, SAXS, cryo-TEM*

A great variety of viral waterborne pathogens are responsible for numerous deaths throughout the globe.[1] In sub-Saharan Africa and South Asia, viruses are a major contributor to the death of up to 700 000 children yearly due to diarrheal diseases.[2] Water treatment, including purification by size exclusion, reduces the impact of pathogens on populations,[1] but purification efficiency is highly influenced by the colloidal structure and stability of viral particles in the nanometer range.[3−6] Moreover coagulation is a well-established water treatment process to remove both natural organic matter (NOM) and particles, by destabilizing their colloidal structures.[7,8] The use of some coagulants such as aluminum salts also contributes to virus removal through inactivation.[9−11] Water chemistry and pH play a role in the efficiency of virus inactivation by aluminum salt coagulants.[10,11] A systematic understanding of the virus−virus interactions from this study will allow an improved mechanistic understanding of the coagulation and adsorption filtration removal of viruses.

Several environmental factors affect virus−virus interaction and their aggregation state, such as salt concentration, their type (monovalent, divalent),[12] and the presence of NOM.[13] The composition of the virus influences its electric charge, resulting in a wide range of isoelectric points (IEP).[14] The electric charge of the particles influences their colloidal behavior. The parameters influencing viral aggregation in aquatic environments have recently been reviewed.[15] Even though the IEP is routinely used to explain the viral aggregation behavior, the impact of pH on the colloidal interactions of viruses has not yet been systematically studied. Hence, the major aim of this study is to understand the effect of pH and presence of NOM on the colloidal structure of viruses using the bacteriophage MS2 as model virus. The MS2 bacteriophage is used as a surrogate due to its small size of around 27 nm and lower isoelectric point than common enteric pathogenic viruses, which indicates MS2 has a higher

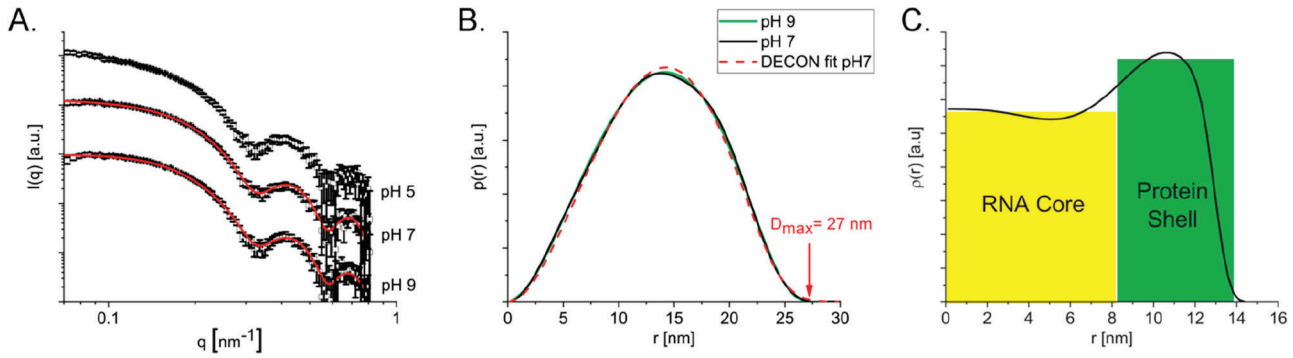

Figure 1. (A) Experimental SAXS data (open squares) and corresponding fits (red curves) calculated using the generalized indirect Fourier transformation method for MS2 in the absence of NOM. (B) Pair distance distribution calculated from data shown in A with eq 5 is shown as a black solid line for pH = 7.0 and green for pH = 9.0. The fit calculated from the deconvolution for pH = 7.0 with a convolution square root operation is shown as a red dashed line. (C) Radial excess electron density of the virus at pH = 7.0, calculated by the deconvolution of part B.

colloidal stability at lower pH.[14,16] Further, MS2 is a well-established model when investigating viral removal in water filtration processes,[17−19] as well as coagulation processes.[20]

MS2's structure in vacuum has been determined, by XRD on virus crystals, to be a 26−28 nm quasi-spherical particle with a positive-sense single-stranded RNA core and a protein shell.[21,22] The protein shell, also called a capsid, was determined to be composed of three different peptides creating a repeating subunit; each capsid is composed of 60 subunits.[21,22] The RNA core is bound by a hairpin operator to the capsid.[23] Advances in cryogenic transmission electron microscopy (cryo-TEM)-based reconstructions elucidated, under vitrified conditions, a branched network of stem-loop RNA structures that bind the capsid proteins.[24,25] Through single particle asymmetric reconstruction techniques, cryo-TEM imaging allowed refining the capsid structure with the single A-protein and 178 capsid proteins[25] instead of the 180 capsid proteins previously resolved by XRD. The A-protein could not be crystallized, however is of high biological relevance since it may bind the bacteria during the infection cycle.[26]

The structure has also been investigated in solution, at pH = 7 and high ionic strength (100 mM NaCl and 1 mM $MgCl_2$), with scattering techniques. Small-angle X-ray scattering (SAXS) with a spherical core−shell form factor model determined that MS2's structure has an RNA core radius of 83 ± 1 Å and a protein shell radius of 134 ± 2 Å.[27] Additionally, small-angle neutron scattering has determined MS2's core to be composed of 27 ± 2 wt % RNA.[28]

Dynamic light scattering (DLS) at different time points and SAXS showed, at pH = 7 in the presence of 50 mM Ca^{2+}, the dominant attractive interactions between MS2 particles, whereas repulsive interactions were shown, qualitatively, at pH = 7 in the presence of monovalent cations.[12] The structure studies of MS2 in solution have, up to now, been performed at pH = 7. However, change in water pH is an important environmental factor and has been known to influence virus colloidal stability as well as being used to concentrate virus through pH-dependent adsorption processes since the 1980s.[29] Hence, the effect of pH variation on the particle's structure and more importantly their interactions is understudied.

This study demonstrates the pH-responsive colloidal structure of MS2 in water and the impact of NOM on virus self-assembly. SAXS in combination with model-independent reconstruction of the structure of MS2, dynamic light scattering, and cryo-TEM are used to study, in a quantitative fashion, the mechanisms at play behind virus aggregation and disaggregation upon pH change and addition of NOM.

RESULTS AND DISCUSSION

MS2 Structure in Water and Colloidal Interactions. To investigate the effect of pH on MS2 bacteriophages' colloidal structures and interactions, the SAXS curves for the MS2 at pH = 5.0, 7.0, and 9.0 in the absence of NOM have been measured and are presented in Figure 1A. The $I(q)$ at pH = 5.0 shows an upturn at low q values, which may arise from aggregation of the virus particles to aggregates that are larger than 78.5 nm (the resolution limit of the SAXS setup). However, the $I(q)$ at higher q values (q > 0.2 nm^{-1}) are comparable for the three samples, indicating no major change in the structure of the individual virus particles upon pH variation. The larger hydrodynamic diameter of 94.5 nm with a polydispersity index (PDI) of 0.28 at pH = 5.0 agrees with the presence of larger particles, and the wide distribution of sizes implies the aggregation of smaller particles (see Figure 2). The corresponding DLS correlation functions are shown in the

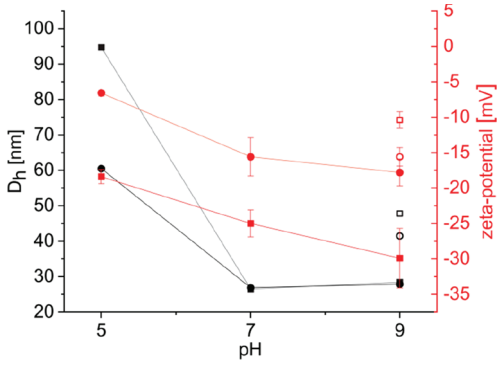

Figure 2. Hydrodynamic diameters from DLS using the cumulant method, are presented in black on the left axis; MS2 (black squares) and MS2 with 10 mg/L NOM (black circles). The ζ-potentials are presented in red on the right axis; MS2 (red squares) and MS2 with 10 mg/L NOM (red circles). Each ζ-potential value corresponds to an average of 3 measurements. The disaggregated MS2 are presented as open symbols. All corresponding correlation functions are presented in the Supporting Information as Figure S1.

http://doc.rero.ch

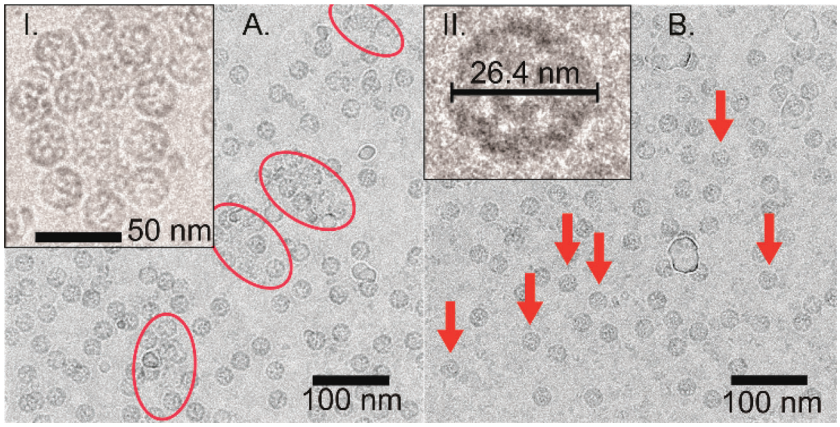

Figure 3. (A) Cryo-TEM image of MS2 at pH = 5.0 in water. Aggregates are highlighted within red circles. Inset I shows an enlarged view of an aggregate. (B) Cryo-TEM image of MS2 at pH = 9.0 in the absence of NOM with examples of single particles indicated by arrows. Inset II shows an enlarged view of a single MS2 virus particle.

http://doc.rero.ch

Supporting Information as Figure S1. The presence of aggregates is further confirmed by cryo-TEM in Figure 3A. The individual particles composing the imaged aggregates can be estimated to have a diameter of around 25−27 nm. Hence, at pH = 5.0 the repulsive interactions are not sufficient to fully hinder aggregation, leading to the distribution of aggregates and single particles.

The shape of the $I(q)$ functions with characteristic maxima and minima and a Guinier region at low q values for the virus at pH = 7.0 and 9.0 suggest nanometer-sized particles well within the resolution range of the SAXS setup. The corresponding $p(r)$ functions for the virus particles at pH = 7.0 and 9.0, shown in Figure 1B, indicate that the virus particles are of approximate spherical shape with a diameter, D_{max}, of 27 nm, from $p(r) = 0$. The virus particles at pH = 9.0 are also imaged by cryo-TEM, shown in Figure 3B. The size of the particles, estimated from the cryo-TEM images, is around 26.4 nm, in good agreement with the results from SAXS. The particle dimension is also in good agreement with previous structure reconstructions performed by high-resolution methods such as X-ray crystallography[21,22] and cryo-TEM.[24,30,31] To study the particle's morphology, the $p(r)$ was deconvoluted with a convolution square root operation to generate the averaged difference radial electron density distribution of the virus particles relative to the buffer. Figure 1C shows the averaged radial electron density profile for MS2 at pH = 7.0. The point of inflection in the excess electron density profile between the core and shell regions provides an estimated radius of the virus core and shell. The core radius is around 8 nm, and overall particle radius of the MS2 is around 13.5 nm. This radius is in reasonable agreement with the apparent interaction radius from the structure factor at pH = 7.0 and pH = 9.0 presented in the Supporting Information as Table S1 and the radius from the $p(r)$ analysis at $D_{max}/2$ (see Figure 1B). It is noteworthy that although the deconvolution was calculated from the $p(r)$ for pH = 7.0, the calculated $p(r)$ is similar to that at pH = 9.0; hence the radial electron density distribution is comparable in this pH range. The core of the virus, consisting mainly of buffer and only 27 wt % of RNA,[28] may explain the lower core electron density relative to the protein shell. For complementary analysis of the SAXS data, the parameters from the model-free analysis of the scattering data have further been used to calculate the best possible fit to the SAXS data using a spherical core−shell form factor model.[32,33] The calculated curves are in good agreement with the form factor scattering, confirming the meaningful results from the model-free SAXS data analysis. The mathematical model is presented in the Supporting Information, and the parameters and fit are shown in Table S2 and Figure S2 of the Supporting Information.

Additional DLS analysis of the MS2 showed relatively monodisperse particles with a D_H of around 28 nm at pH = 7.0 and 9.0 with a PDI below 0.1, in good agreement with the dimensions obtained from SAXS (see Figure 2). The corresponding correlation functions, presented in the Supporting Information as Figure S1, are characteristic of monomodal particle size distributions with one decay only.

Structure factor analysis was then used to study the interactions between the MS2 particles that drive stabilization and aggregation processes. These interactions can be observed in the $I(q)$ curves from SAXS, showing a slight downturn at pH = 7.0 and a more pronounced downturn at pH = 9.0 in the low-q region ($q < 0.1$ nm^{-1}). The more pronounced downturn at higher pH = 9.0 hints toward stronger repulsion and a more ordered system at pH = 9.0 than at pH = 7.0 in the absence of NOM. In agreement with these observations, ζ-potential measurements showed an increase of the effective charge of the particles from −25.0 mV to −29.9 mV when increasing pH from 7.0 to 9.0 (Figure 2). The higher charge results in stronger electrostatic repulsion forces, preventing aggregation.

A comprehensive analysis of the structure factor from SAXS with the charged sphere model underlines this pH dependence of the repulsive interactions. At approximated effective charge values from ζ-potential measurements reported above, the higher apparent volume fraction of 4.6% at pH = 9.0 (at an apparent charge of −29 mV) compared to 2.7% at pH = 7.0 (at an apparent charge of −25 mV) demonstrates the stronger structure factor contribution to the $I(q)$ at higher pH. This apparent volume fraction is much higher than the estimated virus concentration of around 1 mg/mL, which may be caused by hydration of the proteins and the cage shape of the virus particles, which take up a lot of volume per mass. The effective interaction radius was comparable at both pH values, 18.5 nm at pH = 7.0 and 18.1 nm at pH = 9.0. All fitting parameters are reported in the Supporting Information (Table S2). The protonation state of the amino acids is responsible for the variation of charge with pH,[34] hence the repulsion variations.

When the pH was decreased to pH = 5.0, nanometer size range aggregates were observed as discussed above. Upon

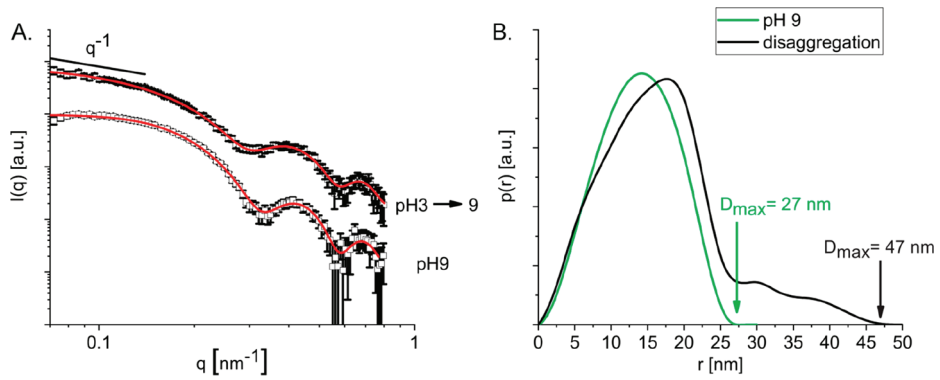

Figure 4. (A) Experimental SAXS data (open squares) and corresponding fits (red curves) calculated using the generalized indirect Fourier transformation method for MS2 after disaggregation through pH increase from 3.0 to 9.0 and native particles at pH = 9.0. (B) Corresponding pair distance distribution functions calculated from the data shown in A with eq 5.

http://doc.rero.ch

further decease in the pH to 3.0, the aggregate size increased to the micrometer size range, observed as a visible phase separation. Interestingly, when the pH was recirculated to pH = 7.0 and 9.0 upon addition of NaOH, the solution became transparent again, as shown with the photographs in the Supporting Information as Figure S3. This transition from the macroscopic virus aggregates to nanoparticles was almost spontaneous upon pH increase, and minimum agitation for pH equilibration. However, the D_H of the sample measured with DLS after disaggregation was 40 nm, with a PDI of 0.31, which was larger than the D_H of the initial sample of 28 nm with a PDI of 0.05 at pH = 9.0 (see Figure 2). This may result from coexisting populations of individual virus particles with virus debris and aggregates such as dimers.

The $I(q)$ curves of disaggregated virus particles, presented in Figure 4A, have shallower minima, indicating a more polydisperse system than native virus particles at pH = 9.0, in agreement with the results from DLS. The shape of the SAXS $I(q)$ with a q^{-1} dependence in the low-q region ($q < 0.1$ nm^{-1}) indicates the presence of virus aggregates of apparent cylindrical shape (*i.e.*, dimers).[35] To better understand the particles' size and shape, the $p(r)$ was calculated from the $I(q)$ and is shown in Figure 4B with the corresponding structure factor parameters presented in Supporting Information (Table S2). The shape of the $p(r)$ with a tailing off to larger r values also indicates a deviation from the approximate spherical shape to more elongated structures. This suggests the presence of virus aggregates with a length of 47 nm (estimated from $p(r) = 0$) and an estimated diameter of 27 nm, comparable to an aggregate composed of two viruses. The maximum dimension from SAXS is a lower estimate, as it appears above the resolution limit of the setup. Cryo-TEM analysis of this sample showed a population composed of small aggregates and single virus particles as shown in Figure 5A. A representative virus dimer from this sample is presented in Figure 5B. The dimensions of this dimer with a diameter of around 27 nm and length of 52 nm are in reasonable agreement with the values obtained from SAXS analysis.

Effect of NOM on MS2 Interactions. In the presence of NOM, the $I(q)$, presented in Figure 6A, are comparable to those in the absence of NOM, indicating no substantial change in the virus size, shape, and morphology upon NOM addition. At pH = 5.0, the presence of aggregates larger than the resolution limit of the SAXS setup is indicated by an upturn at low q values. Upon addition of NOM, the D_H from DLS analysis at pH = 5.0 was found to decrease from 94.5 nm (PDI = 0.24) to 60.5 nm (PDI = 0.28) with an increase in the ζ-potential from −18.4 mV to −6.6 mV (see Figure 2). The cryo-TEM image of this sample shows aggregates composed of individual virus particles with a diameter of around 25−27 nm (see Figure 7A).

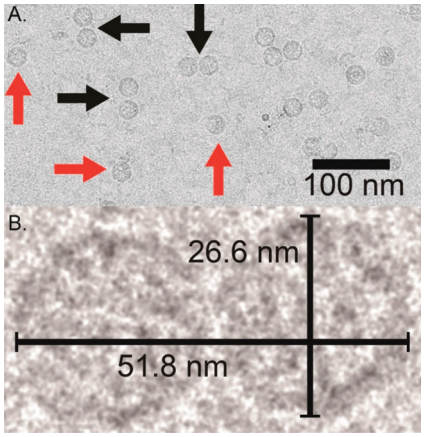

Figure 5. (A) Cryo-TEM image of MS2 at pH 9.0 after aggregation at pH = 3.0, supporting the SAXS data from this sample in Figure 4. Virus dimers that may appear as ellipsoidal structures in the SAXS profile are indicated with black arrows and single viruses with red arrows. Additional images of this sample can be found in Figure S4 in the Supporting Information. (B) Enlarged view of a virus dimer with dimensions.

The SAXS data for the virus nanoparticles at pH = 7.0 and 9.0, presented in Figure 6A, show that the shape of the $I(q)$ functions in the presence of NOM presents similar positions for the minima and maxima to those in the absence of NOM. However, the minima are slightly shallower, indicating higher polydispersity, possibly due to the adsorbed NOM coating of the virus particles. The corresponding $p(r)$ functions for the virus particles at pH = 7.0 and 9.0 in the presence of NOM are shown in Figure 6B and indicate the virus particles are of approximate spherical shape with a diameter, D_{max}, of 27 nm, from $p(r) = 0$ in the presence of NOM. Hence, the structure of the virus particles at pH = 7.0 and 9.0 appears not to be significantly impacted by the addition of NOM. The cryo-TEM image of this sample confirms the presence of nanoparticles of approximate spherical shape and diameter of around 25 nm (Figure 7B), and the inset shows a 25.2 nm particle. Further DLS data recorded at pH = 7.0 and 9.0 in the presence of NOM show a D_H of about 27 nm at PDI < 0.1,

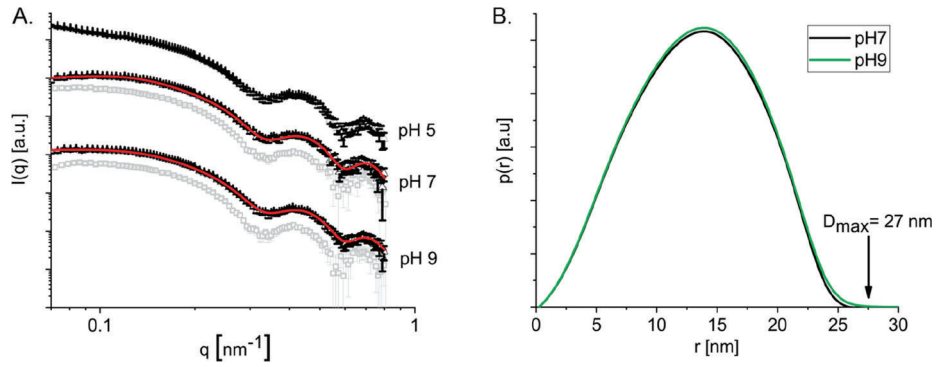

Figure 6. (A) Experimental SAXS data in the presence of 10 mg/L NOM (open black triangles). SAXS data in the absence of NOM are also included with open gray squares for comparison. The fits calculated with the generalized indirect Fourier transformation method are shown as red lines. (B) Corresponding pair distance distribution functions calculated from data shown in A with eq 5.

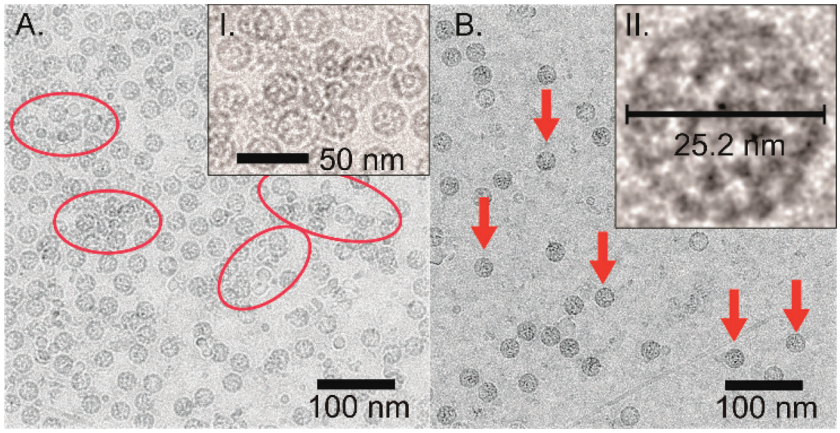

Figure 7. (A) Representative cryo-TEM image of MS2 at pH = 5.0 in the presence of NOM. Aggregates are highlighted within red circles. Inset I shows an enlarged view of an aggregate. (B) Cryo-TEM image of MS2 at pH = 9.0 in the presence of NOM. Examples of single particles are indicated by arrows. Inset II shows an enlarged view of a single MS2 virus particle.

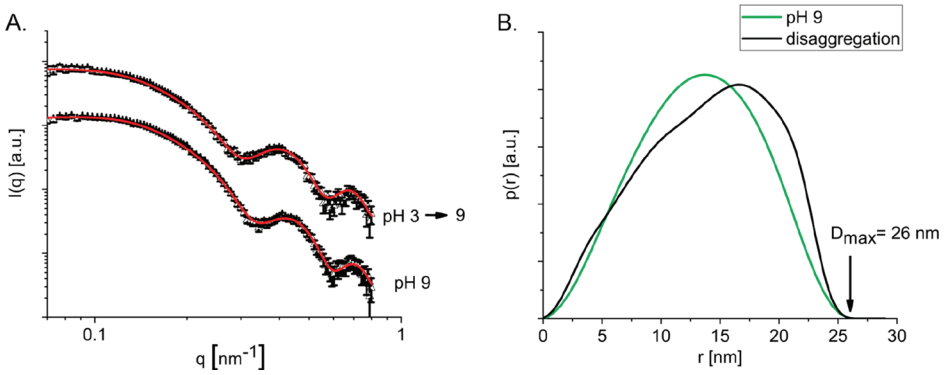

Figure 8. (A) Experimental SAXS data (open squares) and corresponding fits (red curves) calculated with the generalized indirect Fourier transformation method for MS2 after disaggregation and at pH = 9.0. The structure factor parameters are presented in the Supporting Information, Table S2. (B) Corresponding pair distance distribution function calculated from data shown in A with eq 5.

similar to the sample in the absence of NOM. Repulsive interactions between the virus particles at both pH values are indicated in the $I(q)$ curves by a downturn in the low-q region (q < 0.1 nm^{-1}). The structure factor parameters from SAXS analysis, presented in the Supporting Information (Table S2), demonstrate stronger repulsive interaction and increased stability to pH variation than in the absence of NOM: The apparent volume fractions, calculated at the effective charge from the ζ-potential measurements, were around 7% for pH = 7.0 (at an apparent charge of −15.6 mV) and 8% for pH = 9.0 (at an apparent charge of −17.8 mV), almost double the values reported for virus particles in the absence of NOM. The apparent interaction radii of around 22 nm for both pH values are larger than the one for virus particles in the absence of NOM.

The effect of NOM on virus stabilization is further studied by aggregating the virus at pH 3.0 and disaggregating by increasing the pH to 9.0. Contrary to the system in the absence of NOM, where aggregates were dominating the SAXS pattern, the $I(q)$ curve after disaggregation in the presence of NOM is

http://doc.rero.ch

characteristic for nanoparticles with a Guinier region[32] at low q values (see Figure 8A). Hence the particles tend to disperse more efficiently in the presence of NOM. The minima in the $I(q)$ of the disaggregated viruses appear shallower and shifted to lower q values compared to the one before aggregation due to increased polydispersity, which could be caused, for instance, by the presence of some minor population of virus debris. The corresponding $p(r)$ suggests an approximate spherical shape of the particles with a D_{max} of 26 nm, as presented in Figure 8B. The $p(r)$ of the disaggregated particle has a maximum shifted to higher r values (about 17 nm) compared to the native particles (maximum at r about 14 nm) and a sharper decrease to $p(r) = 0$. This indicates a change in excess electron density in the virus core. Similar $p(r)$ profiles were simulated for hollow spheres.[35] The hollower structure of the virus particle after disaggregation may be explained by the potential loss of RNA from the core region during the aggregation at pH = 3.0, leading to a decrease in excess electron density in the core region.[36] However, one has to consider that the bulk electron density might increase upon addition of NOM due to the solvation of some of the species in the bulk. Further, additional side maxima in the $p(r)$ can be seen that indicate a convolution of the virus particle $p(r)$ with that of coexisting virus debris such as free RNA or protein fragments. Hence, meaningful results for radial excess electron density profiles cannot be obtained by deconvolution for this sample. These additional features are present in the $p(r)$ of the disaggregated particles with and without NOM, indicating similar particle damage by pH circulation between 3.0 and 9.0 in both cases. The results agree well with the DLS findings, showing a higher D_H of 41.5 nm and PDI of 0.31 after disaggregation; see Figure 2. The virus particles in the presence of NOM are further imaged by cryo-TEM and presented in Figure 9A, and a 24.5 nm single particle is shown in Figure 9B.

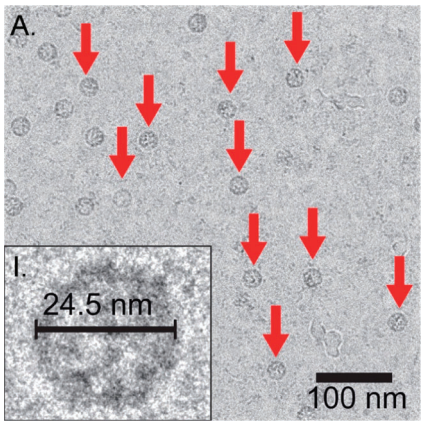

Figure 9. (A) Cryo-TEM image of MS2 after disaggregation in the presence of NOM at pH 9.0. Single viruses are indicated with red arrows. I: Enlarged intact virus from A.

The enhanced stabilization of the virus particles in the presence of NOM suggests that NOM increases the energy barrier to aggregate the particles and destabilizes the virus aggregates at low pH, thus promoting disaggregation. The reduced effect of pH on interactions suggests that the viruses are coated with NOM; hence the increased repulsion in the presence of NOM may be due to interactions between the NOM coatings, potentially through a combination of electrostatic and steric interactions between surface-active NOM components. NOM also prevents virus aggregation when electrostatic interactions are shielded by ions,[12] further underlining the nonelectrostatic nature of the repulsion's enhancement. This result agrees with recent reports on NOM layer formation on charged ZnO nanoparticles that promotes their disaggregation above their isoelectric point through electrostatic and steric interactions.[37]

Implications and Applications of pH-Dependent Virus Colloidal Stability. The results on MS2's interactions show a strong dependence on the water's pH and the presence of NOM. Along with hydrophobicity of the nanoparticle and electrostatic screening,[38] the pH dependence of the interactions has implications for a number of virus−material interactions.

First, the stronger electrostatic repulsions between MS2 nanoparticles at a pH above 7.0 may contribute to the lower observed coagulation efficiency at pH = 8.0 than pH = 7.0 and 6.0 of bacteriophages Qβ and MS2 by aluminum salts.[10] Second, it may also explain the adsorption of MS2 on a noncharged hydrophobic model surface, which is high at pH = 5.0 and 6.0 and drops when pH = 7.0 and 8.0.[34] Finally, for the adsorption of MS2 on polymer cationic brushes, a high initial rate to saturation was observed at high electrostatic interaction, whereas at low electrostatic interaction a lower initial rate but no saturation occurred.[39] The saturation may be caused by the strong repulsion and the absence of saturation at low electrostatic interaction due to the possibility of MS2 aggregation as shown at pH = 5.0.

The aggregation−disaggregation process of the MS2 bacteriophage has also a few relevant implications. First, the possibility to filter by microfiltration micrometer aggregates by size exclusion at low pH and regenerating the filter by washing with alkaline solution. Second, the pH-dependent aggregation−disaggregation process could be used to purify the virus particles from a complex mixture by pH-triggered aggregation, sedimentation, and resuspension at pH = 7.0 or above. Third, ingested viruses transit through the digestive system. The stomach's acidity (pH around 1 to 4)[40] may aggregate viruses, hence protecting the viruses at the center of the aggregate from the protein degrading enzymes such as pepsin and trypsin. The small intestine is more alkaline (pH = 6 to 8)[40] in these conditions, and the viruses may disperse and efficiently infect their host.

Bacteriophage detection and enumeration by common plaque assays will be influenced by the aggregation state of the nanoparticles since virus aggregates will appear as a single plaque when enumerated using plaque assay.[41] The water conditions need to be monitored and possibly modified to hinder virus aggregation before such an assay, particularly for viruses with isoelectric points close to the pH of solutions used for dilution and/or enumeration.

CONCLUSION

MS2 bacteriophage interparticle interactions were found to be highly pH dependent. At pH = 5.0 aggregates are observed in the presence and absence of NOM. At pH = 7.0 and 9.0 elevated ζ-potentials and repulsive interactions were recorded with SAXS. At these pH values, virus nanoparticles with a diameter of around 27 nm were observed by SAXS, cryo-TEM, and DLS. The pH-dependent virus aggregation process at low pH = 3.0 was also found to be reversible upon pH increase to 7.0 and 9.0. NOM was found to promote the virus disaggregation to single particles. In this context, NOM

http://doc.rero.ch

increases the stability of the virus particles at low pH and may thus impact coagulation and filtration processes. Nonetheless tailoring the colloidal structures by pH control may help improve water treatment processes. Coagulation and adsorption filtration will have higher adsorption rates at higher pH but will have limited capacity due to the high virus−virus repulsions. On the other hand more viruses will be adsorbed at low pH at a lower rate, but virus leaching is a risk if the pH is increased.

MATERIALS AND METHODS

Virus Propagation. MS2 (DSMZ 1367, DSMZ, Germany) was replicated in *Escherichia coli* strain W1485 (DSMZ 5695, DSMZ, Germany). *E. coli* was incubated in broth, the composition is given in Supporting Information, at T = 37 °C at 80 rpm (Multitron, Infors-ht, Germany). When the bacteria culture reached an optical density of 0.04 (Genesys 6, ThermoSpectronic, USA), it was infected with MS2 at a ratio to *E. coli* of 0.1 (multiplicity of infection). The infected bacteria were further incubated for 4−5 h at T = 37 °C without shaking (Multitron, Infors-ht, Germany).

Virus Purification and Sample Preparation. Bacterial debris was removed by centrifugation at 2600g for 20 min (Eppendorf 5810R, Eppendorf Germany). The phage-containing supernatant was filtered with 0.22 μm sterile filters (MillexGP, Millipore, Ireland) to remove any remaining bacterial debris. The flow-through was then concentrated from 7 L to approximately 5 mL with centrifugal filters (100 kDa Amicon Ultra-15 centrifugal filters, Millipore, Ireland). The MS2 solution was washed with at least 5 L of virus dilution buffer (VDB) at pH = 7.0 (see Supporting Information for composition), by multiple 13−15 mL washing steps in the centrifugal filters. The solution was finally filtered through 0.1 μm sterile filters (MillexVV, Millipore, Ireland), in agreement with the virus purification method previously reported.[34] The virus purity was analyzed by SDS-PAGE (details can be found in the Supporting Information), and gels are presented in Figure S5. The final volume was adjusted to achieve a final MS2 concentration of 10^{14} PFU/mL, corresponding to about 1 mg/mL.

Natural organic matter (IHSS Suwannee River, 2R101N) was dissolved in VDB to a concentration of 10 mg/L. The disaggregated virus samples were produced by aggregating MS2 at pH = 3.0 and disaggregating them at pH = 9.0. All solutions were prepared using ultrapure water (resistivity >18 MΩ cm, purelab chorus 1 analytic, Elga Veolia, High Wycombe, UK), and pH adjustments were done using 0.1 M NaOH (≥99% purity, Carl Roth GmbH, Karlsruhe, Germany) and 0.1 M HCl (ACS reagent grade, Sigma-Aldrich, Buchs, Switzerland).

Dynamic Light Scattering and ζ-Potential Measurements. DLS was used to determine the mean hydrodynamic diameter (D_H) as well as the polydispersity index. Measurements were made using a Malvern Zetasizer Nano ZS90 (Malvern Instruments, USA) with a He−Ne laser beam at a wavelength of 633 nm. The measurements were performed at a scattering angle of 90° and with a laser power of 4 mW. The temperature was kept at 25 °C in all measurements. The correlation function was fitted with the cumulant method to determine the diffusion coefficient (D).[42] The D_H was determined by D using the Stokes−Einstein equation:[43]

$$D_H = \frac{k_B T}{3\pi\eta D} \tag{1}$$

where k_B is the Boltzmann constant, T the absolute temperature (298.15 K), and η the viscosity of the solvent (water, 0.8919 mPa·s). The PDI of the size distribution is determined from the second cumulant:

$$\mathrm{PDI} = \frac{\mu_2}{\bar{\Gamma}^2} \tag{2}$$

where μ_2 is the second cumulant and $\bar{\Gamma}$ is the mean inverse decay time.

Small-Angle X-ray Scattering. SAXS patterns were collected on a Bruker Nanostar (Bruker AXS, Karlsruhe, Germany) connected to an X-ray source (Incoatec IμSCu, Geesthacht, Germany) operating at 50 kV and 600 μA with a sealed tube Cu anode. A Göbel mirror was used to convert the divergent polychromatic X-ray beam into a focused beam of monochromatic Cu Kα radiation (λ = 1.54 Å). The beam cross-section diameter was 0.3 mm. A sample-to-detector distance of 107.5 cm gave the q-range of around 0.07 < q < 1 nm^{-1}, where q is the length of the scattering vector, defined by

$$q = \left(\frac{4\pi}{\lambda}\right)\sin\left(\frac{\theta}{2}\right) \tag{3}$$

where λ is the wavelength and θ is the scattering angle. The 2D SAXS patterns were acquired within 1 h using a VÅNTEC-2000 detector (Bruker AXS, Karlsruhe, Germany) with an active area of 14 cm × 14 cm and a pixel size of 68 μm × 68 μm.

The scattering curves were corrected for absorption using a semitransparent beamstop. Buffer scattering was subtracted as background from all samples.

SAXS Data Analysis. The scattering intensity $I(q)$ of N monodisperse, homogeneous, and spherical particles is a product of their form and structure factor scattering, $P(q)$ and $S(q)$:

$$I(q) = NS(q)\,P(q) \tag{4}$$

The generalized indirect Fourier transformation method allows the simultaneous fitting of $P(q)$ and $S(q)$ by selecting a suitable $S(q)$ model.[44−47]

The pair density distribution function, $p(r)$, that provides direct information on size and shape of the particles can be calculated from $P(q)$ *via*[48,49]

$$P(q) = 4\pi\int_0^\infty p(r)\frac{\sin(qr)}{qr}\mathrm{d}r \tag{5}$$

where

$$p(r) = r^2\Delta\tilde{\rho}^2(r) \tag{6}$$

with $\Delta\tilde{\rho}^2(r)$ being the convolution square of the spatially averaged excess electron density $\Delta\rho(r)$.

In the case of spherical geometry, deconvolution of the $p(r)$ gives the radial contrast profile in electron density $\Delta\rho(r)$ relative to the mean value, which gives information about the internal structure of the scattering particles.[50,51]

The effective interparticle structure factor for charged spheres was simultaneously calculated using the Yukawa potential (screened coulomb potential)[52,53] with the hypernetted chain closure relation.[54] The interaction radius and the volume fraction were modeled, whereas the effective charge was estimated from the ζ-potential measurements.

$$V = \frac{Q{e_0}^2}{4\pi\epsilon\epsilon_0}\frac{\exp(-\kappa h)^2}{1+\kappa a} \tag{7}$$

with V being the potential, Q the effective charge, e_0 the charge of an electron, ϵ_0 the permittivity of a vacuum, ϵ the relative dielectric constant, κ the Debye screening, a the particle radius, and h the surface-to-surface distance between the spheres defined by

$$h = r - 2a \tag{8}$$

with a being the particle radius and r the particle center to particle center distance.

The Debye screening length is

$$\kappa^{-1} = \sqrt{\frac{\epsilon_0\epsilon kT}{2N_A{e_0}^2 I}} \tag{9}$$

with N_A being Avogadro's number and I the ionic strength:

$$I = \frac{1}{2}\sum_{i=1}^{n} c_i{z_i}^2 \tag{10}$$

http://doc.rero.ch

with the concentrations c_i and charges z_i of all n ions present in the solution. The data were fitted up to $q = 0.8$ nm^{-1} due to the very low signal-to-noise ratio above that value.

Cryo-TEM. For cryo-TEM analysis 4.0 μL of virus solution at about 1 mg/mL was applied onto Quantifoil R2/1 300 (Quantifoil, Großlöbichau, Germany) mesh copper grids, which were previously negatively glow-discharged at 25 mA for 30 s. Excess of sample was blotted away for 2 s and plunge-frozen into a liquid ethane/propane (37/63) mixture (continuously cooled by liquid nitrogen to around 77 K) using a Vitrobot Mark IV (ThermoFisher Scientific, USA) with an environmental chamber set to 100% humidity and 22 °C.

Vitrified grids were observed under a Tecnai F20 (ThermoFisher Scientific, USA) electron microscope using a Gatan 626 cryo-holder (Gatan, USA). Falcon 2 (ThermoFisher Scientific, USA) CMOS direct detector integrated micrographs representing a cumulative dose of ~45 electrons per Å^2 were collected at approximately −3 μm defocus and 1.32 Å pixel size with a magnification of 80 000.

The images were analyzed with the analyze particle function in the Fiji[55] distribution of ImageJ[56,57] to retrieve estimations on the size distribution of the particles.

ASSOCIATED CONTENT

Supporting Information

The Supporting Information is available free of charge at https://pubs.acs.org/doi/10.1021/acsnano.9b08112.

Additional information on the broth and virus dilution buffer preparation and the SDS-PAGE method, core−shell form factor model with the corresponding parameters and fit to the form factor scattering, DLS intensity correlation functions, photographs showing the optical appearance of the solutions of aggregated and resuspended MS2, additional cryo-TEM images of the disaggregated MS2, SDS page analysis of the MS2 batches, and parameters for the structure factor model (PDF)

AUTHOR INFORMATION

Corresponding Author

Stefan Salentinig − *Department of Chemistry, University of Fribourg, 1700 Fribourg, Switzerland; Biointerfaces Lab, Empa, Swiss Federal Laboratories for Material Science and Technology, 9014 St. Gallen, Switzerland;* orcid.org/0000-0002-7541-2734; Email: stefan.salentinig@unifr.ch

Authors

Samuel Watts − *Biointerfaces Lab, Empa, Swiss Federal Laboratories for Material Science and Technology, 9014 St. Gallen, Switzerland*

Timothy R. Julian − *Eawag, Swiss Federal Institute of Aquatic Science, 8600 Dübendorf, Switzerland; Swiss Tropical and Public Health Institute, 4002 Basel, Switzerland; University of Basel, 4003 Basel, Switzerland;* orcid.org/0000-0003-1000-0306

Katharina Maniura-Weber − *Biointerfaces Lab, Empa, Swiss Federal Laboratories for Material Science and Technology, 9014 St. Gallen, Switzerland;* orcid.org/0000-0001-7895-3563

Thomas Graule − *High Performance Ceramics Lab, Empa, Swiss Federal Laboratories for Materials Science and Technology, 8600 Dübendorf, Switzerland*

Complete contact information is available at: https://pubs.acs.org/10.1021/acsnano.9b08112

Notes

The authors declare no competing financial interest.

ACKNOWLEDGMENTS

The studies were funded by Empa. The authors acknowledge the Scientific Center for Optical and Electron Microscopy (ScopeM) for technical assistance and access to cryo-TEM facilities. This work benefited from the use of the SasView application.

REFERENCES

(1) Gibson, K. E. Viral Pathogens in Water: Occurrence, Public Health Impact, and Available Control Strategies. *Curr. Opin. Virol.* **2014**, *4*, 50−57.

(2) Kotloff, K. L.; Nataro, J. P.; Blackwelder, W. C.; Nasrin, D.; Farag, T. H.; Panchalingam, S.; Wu, Y.; Sow, S. O.; Sur, D.; Breiman, R. F.; et al. Burden and Aetiology of Diarrhoeal Disease in Infants and Young Children in Developing Countries (The Global Enteric Multicenter Study, GEMS): A Prospective, Case-Control Study. *Lancet* **2013**, *382*, 209−222.

(3) Mattle, M. J.; Crouzy, B.; Brennecke, M.; Wigginton, K. R.; Perona, P.; Kohn, T. Impact of Virus Aggregation on Inactivation by Peracetic Acid and Implications for Other Disinfectants. *Environ. Sci. Technol.* **2011**, *45*, 7710−7717.

(4) Feng, Z.; Lu, R.; Yuan, B.; Zhou, Z.; Wu, Q.; Nguyen, T. H. Influence of Solution Chemistry on the Inactivation of Particle-Associated Viruses by UV Irradiation. *Colloids Surf., B* **2016**, *148*, 622−628.

(5) Kahler, A. M.; Cromeans, T. L.; Metcalfe, M. G.; Humphrey, C. D.; Hill, V. R. Aggregation of Adenovirus 2 in Source Water and Impacts on Disinfection by Chlorine. *Food Environ. Virol.* **2016**, *8*, 148−155.

(6) Sigstam, T.; Rohatschek, A.; Zhong, Q.; Brennecke, M.; Kohn, T. On the Cause of the Tailing Phenomenon During Virus Disinfection by Chlorine Dioxide. *Water Res.* **2014**, *48*, 82−89.

(7) Matilainen, A.; Vepsalainen, M.; Sillanpaa, M. Natural Organic Matter Removal by Coagulation during Drinking Water Treatment: A Review. *Adv. Colloid Interface Sci.* **2010**, *159*, 189−197.

(8) Shon, H. K.; Vigneswaran, S.; Snyder, S. A. Effluent Organic Matter (EfOM) in Wastewater: Constituents, Effects, and Treatment. *Crit. Rev. Environ. Sci. Technol.* **2006**, *36*, 327−374.

(9) Matsushita, T.; Shirasaki, N.; Matsui, Y.; Ohno, K. Virus Inactivation during Coagulation with Aluminum Coagulants. *Chemosphere* **2011**, *85*, 571−576.

(10) Shirasaki, N.; Matsushita, T.; Matsui, Y.; Marubayashi, T. Effect of Aluminum Hydrolyte Species on Human Enterovirus Removal from Water during the Coagulation Process. *Chem. Eng. J.* **2016**, *284*, 786−793.

(11) Shirasaki, N.; Matsushita, T.; Matsui, Y.; Marubayashi, T.; Murai, K. Investigation of Enteric Adenovirus and Poliovirus Removal by Coagulation Processes and Suitability of Bacteriophages MS2 and PhiX174 as Surrogates for Those Viruses. *Sci. Total Environ.* **2016**, *563*−*564*, 29−39.

(12) Mylon, S. E.; Rinciog, C. I.; Schmidt, N.; Gutierrez, L.; Wong, G. C. L.; Nguyen, T. H. Influence of Salts and Natural Organic Matter on the Stability of Bacteriophage MS2. *Langmuir* **2010**, *26*, 1035−1042.

(13) Wong, K.; Mukherjee, B.; Kahler, A. M.; Zepp, R.; Molina, M. Influence of Inorganic Ions on Aggregation and Adsorption Behaviors of Human Adenovirus. *Environ. Sci. Technol.* **2012**, *46*, 11145−11153.

(14) Michen, B.; Graule, T. Isoelectric Points of Viruses. *J. Appl. Microbiol.* **2010**, *109*, 388−397.

(15) Gerba, C. P.; Betancourt, W. Q. Viral Aggregation: Impact on Virus Behavior in the Environment. *Environ. Sci. Technol.* **2017**, *51*, 7318−7325.

(16) Goodridge, L.; Goodridge, C.; Wu, J.; Griffiths, M.; Pawliszyn, J. Isoelectric Point Determination of Norovirus Virus-Like Particles by Capillary Isoelectric Focusing with Whole Column Imaging Detection. *Anal. Chem.* **2004**, *76*, 48−52.

http://doc.rero.ch

(17) Jin, Y.; Chu, Y. J.; Li, Y. S. Virus Removal and Transport in Saturated and Unsaturated Sand Columns. *J. Contam. Hydrol.* **2000**, *43*, 111−128.
(18) You, Y.; Han, J.; Chiu, P. C.; Jin, Y. Removal and Inactivation of Waterborne Viruses Using Zerovalent Iron. *Environ. Sci. Technol.* **2005**, *39*, 9263−9269.
(19) Zhuang, J.; Jin, Y. Interactions between Viruses and Goethite during Saturated Flow: Effects of Solution pH, Carbonate, and Phosphate. *J. Contam. Hydrol.* **2008**, *98*, 15−21.
(20) Meyn, T.; Leiknes, T. O.; König, A. MS2 Removal from High NOM Content Surface Water by Coagulation - Ceramic Microfiltration, for Potable Water Production. *AIChE J.* **2012**, *58*, 2270−2281.
(21) Valegard, K.; Liljas, L.; Fridborg, K.; Unge, T. The Three-Dimensional Structure of the Bacterial Virus MS2. *Nature* **1990**, *345*, 36−41.
(22) Golmohammadi, R.; Valegard, K.; Fridborg, K.; Liljas, L. The Refined Structure of Bacteriophage MS2 at 2.8 A Resolution. *J. Mol. Biol.* **1993**, *234*, 620−639.
(23) Ni, C. Z.; Syed, R.; Kodandapani, R.; Wickersham, J.; Peabody, D. S.; Ely, K. R. Crystal Structure of the MS2 Coat Protein Dimer: Implications for RNA Binding and Virus Assembly. *Structure* **1995**, *3*, 255−263.
(24) Koning, R.; Van den Worm, S.; Plaisier, J. R.; Van Duin, J.; Abrahams, J. P.; Koerten, H. Visualization by Cryo-Electron Microscopy of Genomic RNA That Binds to the Protein Capsid Inside Bacteriophage MS2. *J. Mol. Biol.* **2003**, *332*, 415−422.
(25) Koning, R. I.; Gomez-Blanco, J.; Akopjana, I.; Vargas, J.; Kazaks, A.; Tars, K.; Carazo, J. M.; Koster, A. J. Asymmetric Cryo-EM Reconstruction of Phage MS2 Reveals Genome Structure *In Situ*. *Nat. Commun.* **2016**, *7*, 12524−12529.
(26) Lodish, H. F.; Horiuchi, K.; Zinder, N. D. Mutants of the Bacteriophage F2: V. On the Production of Noninfectious Phage Particles. *Virology* **1965**, *27*, 139−155.
(27) Kuzmanovic, D. A.; Elashvili, I.; Wick, C.; O'Connell, C.; Krueger, S. Bacteriophage MS2: Molecular Weight and Spatial Distribution of the Protein and RNA Components by Small-Angle Neutron Scattering and Virus Counting. *Structure* **2003**, *11*, 1339−1348.
(28) Kuzmanovic, D. A.; Elashvili, I.; Wick, C.; O'Connell, C.; Krueger, S. Quantification of RNA in Bacteriophage MS2-Like Viruses in Solution by Small-Angle X-Ray Scattering. *Radiat. Phys. Chem.* **2006**, *75*, 359−368.
(29) Goyal, S. M.; Gerba, C. P. Viradel Method for Detection of Rotavirus from Seawater. *J. Virol. Methods* **1983**, *7*, 279−285.
(30) Langlet, J.; Gaboriaud, F.; Gantzer, C.; Duval, J. F. L. Impact of Chemical and Structural Anisotropy on the Electrophoretic Mobility of Spherical Soft Multilayer Particles: The Case of Bacteriophage MS2. *Biophys. J.* **2008**, *94*, 3293−3312.
(31) Van den Worm, S. H. E.; Koning, R. I.; Warmenhoven, H. J.; Koerten, H. K.; Van Duin, J. Cryo Electron Microscopy Reconstructions of the Leviviridae Unveil the Densest Icosahedral RNA Packing Possible. *J. Mol. Biol.* **2006**, *363*, 858−865.
(32) Guinier, A.; Fournet, G. *Small-Angle Scattering of X-Rays*; John Wiley and Sons: New York, 1955.
(33) Pedersen, J. S. Analysis of Small-Angle Scattering Data from Colloids and Polymer Solutions: Modeling and Least-Squares Fitting. *Adv. Colloid Interface Sci.* **1997**, *70*, 171−210.
(34) Armanious, A.; Aeppli, M.; Jacak, R.; Refardt, D.; Sigstam, T.; Kohn, T.; Sander, M. Viruses at Solid-Water Interfaces: A Systematic Assessment of Interactions Driving Adsorption. *Environ. Sci. Technol.* **2016**, *50*, 732−743.
(35) Glatter, O. Chapter 4. The Inverse Scattering Problem in Small-Angle Scattering. In *Neutron, X-Rays and Light: Scattering Methods Applied to Soft Condensed Matter*; Zemb, T.; Lindner, P., Eds.; Elsevier: North Holland, 2002; pp 73−102.
(36) Salo, R. J.; Cliver, D. O. Effect of Acid pH, Salts, and Temperature on the Infectivity and Physical Integrity of Enteroviruses. *Arch. Virol.* **1976**, *52*, 269−282.
(37) Mohd Omar, F.; Abdul Aziz, H.; Stoll, S. Aggregation and Disaggregation of ZnO Nanoparticles: Influence of pH and Adsorption of Suwannee River Humic Acid. *Sci. Total Environ.* **2014**, *468−469*, 195−201.
(38) Langlet, J.; Gaboriaud, F.; Duval, J. F.; Gantzer, C. Aggregation and Surface Properties of F-Specific RNA Phages: Implication for Membrane Filtration Processes. *Water Res.* **2008**, *42*, 2769−2777.
(39) Dang, H. T. T.; Tarabara, V. V. Virus Deposition onto Polyelectrolyte-Coated Surfaces: A Study with Bacteriophage MS2. *J. Colloid Interface Sci.* **2019**, *540*, 155−166.
(40) Fallingborg, J. Intraluminal pH of the Human Gastrointestinal Tract. *Dan. Med. Bull.* **1999**, *46*, 183−196.
(41) Langlet, J.; Gaboriaud, F.; Gantzer, C. Effects of pH on Plaque Forming Unit Counts and Aggregation of MS2 Bacteriophage. *J. Appl. Microbiol.* **2007**, *103*, 1632−1638.
(42) Berne, B. J.; Pecora, R. *Dynamic Light Scattering*; Dover Publications: Mineola, 2000.
(43) Aragón, S. R.; Pecora, R. Theory of Dynamic Light Scattering from Polydisperse Systems. *J. Chem. Phys.* **1976**, *64*, 2395−2404.
(44) Brunner-Popela, J.; Glatter, O. Small-Angle Scattering of Interacting Particles. I. Basic Principles of a Global Evaluation Technique. *J. Appl. Crystallogr.* **1997**, *30*, 431−442.
(45) Weyerich, B.; Brunner-Popela, J.; Glatter, O. Small-Angle Scattering of Interacting Particles. II. Generalized Indirect Fourier Transformation under Consideration of the Effective Structure Factor for Polydisperse Systems. *J. Appl. Crystallogr.* **1999**, *32*, 197−209.
(46) Brunner-Popela, J.; Mittelbach, R.; Strey, R.; Schubert, K. V.; Kaler, E. W.; Glatter, O. Small-Angle Scattering of Interacting Particles. III. D2O-C12E5Mixtures and Microemulsions with *n*-Octane. *J. Chem. Phys.* **1999**, *110*, 10623−10632.
(47) Fritz, G.; Bergmann, A.; Glatter, O. Evaluation of Small-Angle Scattering Data of Charged Particles Using the Generalized Indirect Fourier Transformation Technique. *J. Chem. Phys.* **2000**, *113*, 9733−9740.
(48) Glatter, O. A New Method for the Evaluation of Small-Angle Scattering Data. *J. Appl. Crystallogr.* **1977**, *10*, 415−421.
(49) Glatter, O. Evaluation of Small-Angle Scattering Data from Lamellar and Cylindrical Particles by the Indirect Transformation Method. *J. Appl. Crystallogr.* **1980**, *13*, 577−584.
(50) Glatter, O. Convolution Square Root of Band-Limited Symmetrical Functions and Its Application to Small-Angle Scattering Data. *J. Appl. Crystallogr.* **1981**, *16*, 101−108.
(51) Glatter, O.; Hainisch, B. Improvements in Real-Space Deconvolution of Small-Angle Scattering Data. *J. Appl. Crystallogr.* **1984**, *17*, 435−441.
(52) Hansen, J. P.; Hayter, J. B. A Rescaled MSA Structure Factor for Dilute Charged Colloidal Dispersions. *Mol. Phys.* **1982**, *46*, 651−656.
(53) Hayter, J. B.; Penfold, J. An Analytic Structure Factor for Macroion Solutions. *Mol. Phys.* **1981**, *42*, 109−118.
(54) Klein, R.; D'Aguanno, B. Static Scattering Properties of Colloidal Suspensions. In *Light Scattering. Principles and Development*; Oxford University Press: New York, 1996; pp 30−102.
(55) Schindelin, J.; Arganda-Carreras, I.; Frise, E.; Kaynig, V.; Longair, M.; Pietzsch, T.; Preibisch, S.; Rueden, C.; Saalfeld, S.; Schmid, B.; Tinevez, J. Y.; White, D. J.; Hartenstein, V.; Eliceiri, K.; Tomancak, P.; Cardona, A. Fiji: An Open-Source Platform for Biological-Image Analysis. *Nat. Methods* **2012**, *9*, 676−82.
(56) Rueden, C. T.; Schindelin, J.; Hiner, M. C.; DeZonia, B. E.; Walter, A. E.; Arena, E. T.; Eliceiri, K. W. ImageJ2: ImageJ for the Next Generation of Scientific Image Data. *BMC Bioinf.* **2017**, *18*, 529−554.
(57) Schneider, C. A.; Rasband, W. S.; Eliceiri, K. W. NIH Image to ImageJ: 25 Years of Image Analysis. *Nat. Methods* **2012**, *9*, 671−675.

http://doc.rero.ch